AN EVALUATION OF USING METAL FUEL IN LIGHT WATER REACTORS

W. LIU, J. Y.R. RASHID, AND M. KENNARD
Structural Integrity Associates, Inc.
9710 Scranton Rd., Suite 300, San Diego CA 92121

BRIAN WIRTH
University of Tennessee Knoxville

WILLIAM LYON
OKLO Inc.

ABSTRACT

This paper summarizes the modelling of the behaviour of metallic fuel, in particular, a helical geometry fuel design with four-lobe cross-section by Lightbridge Corp, in water reactor environments. The responses of metallic fuel under operational and accident conditions, with either a loss of coolant or a rapid power increase using a few idealized cases, were modelled. In comparison to the ceramic UO_2 fuel, the enhanced safety of metallic fuel is clearly shown in the modelling results of accident conditions. This metallic fuel design has no free volume; therefore, it eliminates several issues such as the cladding lift-off due to over-pressure or the cladding ballooning and burst in accident conditions. The fuel temperature in both operation and accident conditions remain much lower than UO_2 fuel, which lowers the temperature and reduces oxidation of the cladding when the surface heat transfer deteriorates due to the loss of cooling. The cladding stresses under the accident conditions with rapid power changes could increase, but not significantly, due to limited fuel thermal expansion. Modelling results have shown large fuel dimensional changes due to swelling, and this could have implications on the in-reactor exposure limit of metal fuels.

1. Introduction

The use of metallic fuel, commonly uranium alloyed with other elements, in water cooled reactors dates back to the 1950s [1-6]. Since then, ceramic UO_2 became the dominant fuel type in commercial nuclear reactors. In research and marine reactors, the operating experience of metal fuel in water reactors does exist [7][8], but the feasibility in commercial reactors remains unknown.

Metallic fuel has salient technical advantages by reducing fuel temperatures and enhancing safety in accident conditions [9]. With appropriate fuel designs, minimal modifications of core design would be needed for its deployment in the LWRs. Given the challenges and known issues of UO_2 fuel, particularly its performance at high burnup conditions, it is worthwhile to assess metal fuel as an alternative to ceramic UO_2 for LWRs.

In the current study, we focus on the fuel design proposed by Lightbridge Corp. Material and geometric information of the fuel design were based on several patents, papers, and presentations [10-16].

The metal fuel design by Lightbridge Corp. as shown in Figure 1 features a multi-lobe geometry with a helical twist along the axial direction. The fuel rod consists of a fuel core, displacer, and a barrier (cladding) to prevent the release of fission products. The fuel core is made of δ-phase U-Zr_2, which is metallurgically bonded to the Zr-Nb alloy cladding, and there is no free volume (gap or plenum) in the fuel rod.

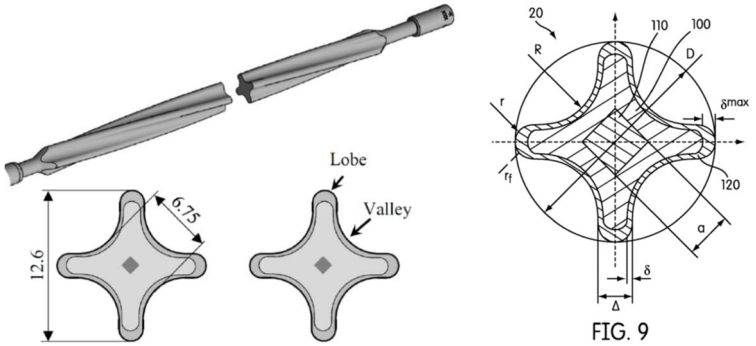

Figure 1: Schematic of Lightbridge metallic fuel design [10] [12]

Table 1 lists the design characteristics range and one set of example parameters, which are used for the modeling work performed in this paper.

Table 1: Design characteristics for Lightbridge metallic fuel

Symbol*	Unit	Characteristic	Range	Example
D	mm	Major Diameter Across Lobes	9 – 14	12.6
Δ	mm	Thickness of Lobes	2.5 – 3.8	3.06
r	mm	Outer Radius of Cladding at Lobe	Δ/2, Δ/1.9	1.53
r_f	mm	Inner Radius of Cladding at Lobe	0.5 – 2.0	1.2
δ_{max}	mm	Thickness of Cladding at Ends of Lobes	0.4-2.2	1.02
d	mm	Thickness of Cladding at Valleys	0.4 – 1.2	0.40
R	mm	Radius Defining Outer Curvature at Valleys	2 - 5	2.97
a	mm	Displacer Width (i.e., Side Length)	1.5 – 3.5	1.56
	mm	Fuel Element Perimeter	25 - 60	40.16
	mm^2	Fuel Core Area	30 – 70	37.49

**Symbols are shown in Figure 1.*

2. U-Zr Material Models

This section describes the thermal and mechanical property models of U-Zr fuel material used for the modelling of metal fuel.

2.1 Thermal Conductivity

Based on a weighted average of data obtained from the INL metal fuels handbook [17] for U-64 at% Zr [18] and U-72 at% Zr [19], a thermal conductivity model was developed by UTK. The thermal conductivity fit to the fresh fuel was performed, assuming a similar polynomial expansion to temperature, and then prescribed with a non-dimensional density dependence, to account for thermal conductivity degradation due to burnup. The resulting equation is given by:

$$k\left(\frac{W}{m\text{-}K}\right) = \frac{\left(3.29 + 6.2 \times 10^{-3}T + 1.55 \times 10^{-5}T^2\right) \times \rho(\text{burnup})}{\rho_0} \quad \text{(Eq. 1)}$$

w here ρ is the density of metal fuel and subscript 0 represents the initial value.

2.2 U-Zr Creep

Creep tests on U-50 wt% Zr alloy were reported by Kutty et al. [20]. In the study, the creep test was performed using the impression method. The temperature ranged from 525 to 575°C, and the stress ranged from 13 to 37 MPa. The average activation energy was given as 106 kJ/mol [20]. The test however covers only a very limited temperature range, and an extrapolation of the model to a wider temperature range was a few orders of magnitude

higher than the fast reactor U-Pu-Zr fuel. Since the creep measurement data for δ-phase U-Zr alloy is very limited, we expanded the data to include higher zirconium alloy (> 60 wt% Zr) for the creep model development. The resultant power law model is shown in Eq. 2.

$$\dot{\varepsilon} = A\exp(-\frac{Q}{RT})\sigma^n \qquad \text{(Eq. 2)}$$

where, A = 0.0041328, Q=210 kJ/mol, n = 4.4715, R=8.314 J/mol-K, T is temperature (K), and σ is stress (MPa).

2.3 Elastic Modulus

The elastic modulus E (GPa) in the δ-phase is a linear fitting to the reported data on arc-melted and induction-melted samples at different temperatures in Ref. [6]. The equation for the elastic modulus is a function of temperature T(K):

$$E = -0.0492\ T + 144.46 \qquad \text{(Eq. 3)}$$

The applicable temperature range is 295 K - 753 K. A reduction of modulus is assumed which yields a 30% reduction of modulus in the γ phase. A constant Poisson's ratio of 0.32 is used in the analysis.

2.4 Thermal Expansion

The heat treatment, composition, and preferred grain orientation can all affect the thermal expansion. Ref. [6]. reported the mean coefficient of thermal expansion (CTE) of δ-phase U-Zr alloy measured at different temperature ranges for two types of test specimens with different heat treatments and compositions (60 wt% and 50 wt% Zr).

Ref. [21] reported the CTE for as-cast and heat treated (550℃ for 24 hrs followed by quench) samples with composition of U-50 wt% Zr, U-60 wt% Zr, and U-70 wt% Zr. In the temperature range of 30 to 600℃, the mean CTE is 4.24×10^{-6} (1/K) for heat treated U-50 wt% Zr. As-cast material, however, shows higher thermal expansion and unstable behaviors.

Using measurement data in Ref. [6] on the U-50 wt% Zr alloy, a fitting was performed and the resultant equation for the linear thermal expansion strain is:

$$\frac{\Delta L}{L}\% = \begin{cases} 4.0\times10^{-7}T^2+7.68\times10^{-4}T-0.020759 & T\le 615\ ℃ \\ 6.76\times10^{-3}T-3.5551 & 615℃<T\le 631\ ℃ \\ 1.445\times10^{-3}T-1.9859\times10^{-3} & T>631\ ℃ \end{cases} \qquad \text{(Eq. 4)}$$

where T is temperature in ℃. The applicable temperature range is 20 to 1000℃.

2.5 Irradiation Swelling

The volumetric strain due to solid fission product swelling is assumed to be proportional to burnup:

$$\varepsilon_s = C \cdot Bu \qquad \text{(Eq. 5)}$$

C is a constant value and *Bu* is burnup in FIMA.

Data on the swelling of δ-phase U-Zr alloy is scarce. Most of those irradiation experiments were conducted at low burnups and low irradiation temperatures [6]. According to [22], the swelling rate for δ-phase U-Zr fuel is 1% per 1%FIMA. This is close to 1.06% per 1% FIMA in a theoretical estimation assuming substitution in solid solution and elastic deformations around fission atoms [5]. This low swelling rate was reported at 280°C with a burnup of 1.75% FIMA [5]. Assuming the fuel swelling for the δ-phase U-Zr is similar to the high zirconium alloys, it was estimated that the solid fission product swelling is 2 to 2.5% per 1% FIMA for the high zirconium alloy [6]. The solid swelling rate used in the current analysis assumes 1.5% per 1% FIMA.

The gaseous swelling model was developed with a number of key assumptions resulting from limited data in the literature for δ-phase U-Zr. The resulting xenon diffusivity and δ-phase U-Zr physical properties were modeled using the Nyx simplified fission gas diffusion and bubble formation model [23][24], which includes xenon intragranular bubble formation and xenon diffusion to the grain boundaries, using a range of xenon diffusivity values to assess the anticipated uncertainty in the point defect super-saturation. The results of the Nyx simulations were then used to populate an engineering scale model of fission gas bubble swelling.

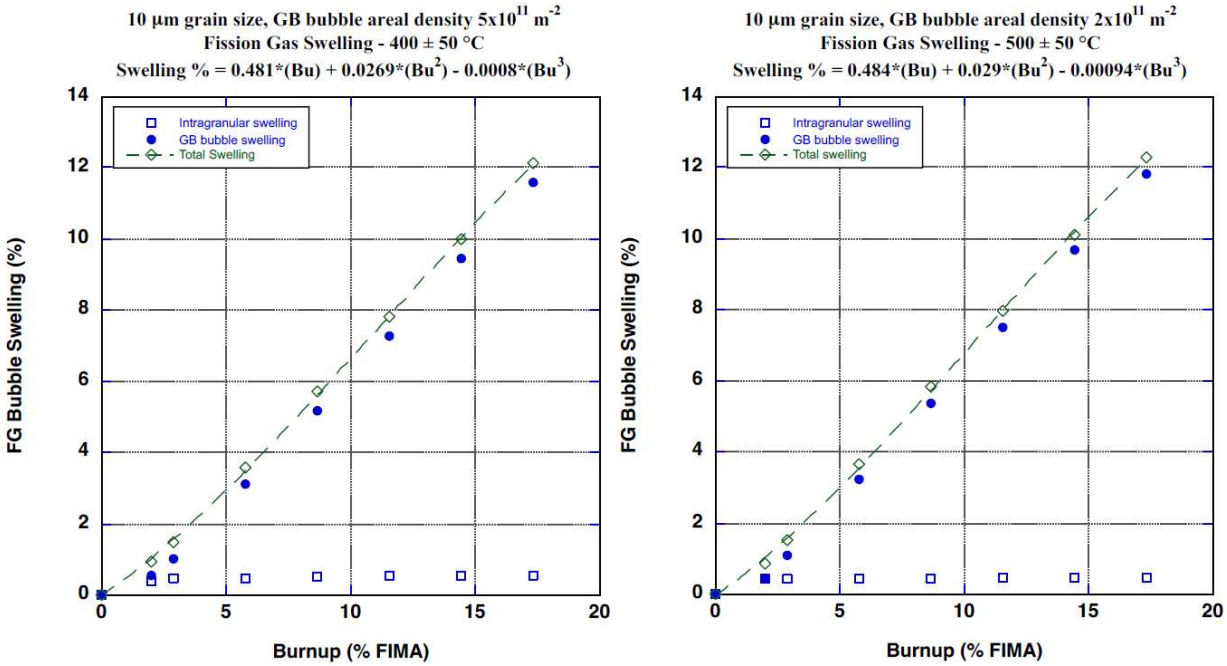

Figure 2: Model of gaseous swelling rate versus burnup for 10 μm grain size

It is important to note that, as a result of the predicted high xenon diffusivity and small grain sizes, the Nyx model indicated that xenon transport to the grain boundaries should dominate the fate of the xenon, relative to the formation of intragranular bubbles. Figure 2 presents the resulting fission gas swelling model, and indicates significant predicted swelling that is dominated by the intergranular bubbles.

In the operating temperature regime, the gaseous swelling model is insensitive to the temperature, and the fitting at 400°C is used as the default. That would give a total fuel swelling rate of 2-3% per 1% FIMA.

3. Modelling Results

This metal fuel design is a four-lobe geometry twisted around and extruded along the axis normal to the four-lobe plane. To model the full-length fuel rod response, the 2-D planar geometry is duplicated along the rod length direction with appropriate thermal and mechanical boundary conditions in each plane geometry at different axial locations to account for the axial variation in the linear power and coolant conditions.

A 3-D segment finite element mesh was created for modeling the local fuel response. Uniform strains are assumed at the top and bottom planes of the rod segment and corresponding boundary condition is applied in BISON input. Figure 3 shows (a) 2-D plane, and (b) 3-D segment meshes respectively. Along the length of the fuel rod, at certain axial locations, the rod-to-rod contact would constrain the lateral movement of neighbor rods. A shroud outside of the fuel assembly would hold all fuel rods and provide the constraint of the lateral displacement of all fuel rods at the rod-to-rod contact planes. To account for this, the boundary conditions at those planes in 3-D or in the 2-D models are added to constrain the lateral movement of the fuel rod.

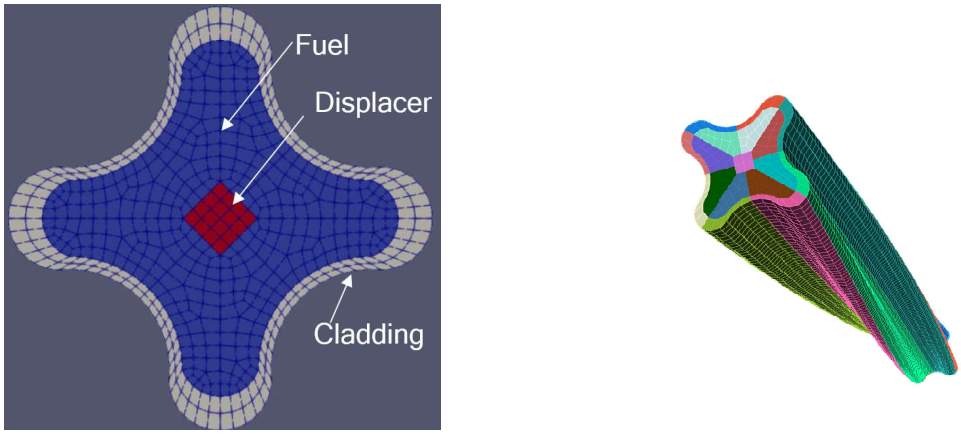

(a) 2-D Plane (b) 3-D Segment

Figure 3: Finite element mesh for the helical four-lobe metal fuel

3.1 Results for Normal Operation

A base case is created by modification of the irradiation history and operating conditions for a PWR UO_2 fuel rod. The linear power and axial power profiles are shown in Figure 4. A equivalent UO_2 fuel under such a power history would have a rod average burnup of 81 GWd/tU, which is 30% higher than the current licensing limit.

A total of 20 2-D X-Y planes are equally distributed along the longitudinal direction of the fuel rod. Those planes are modeled using the generalized plane strain formulation in BISON to represent local fuel slices sampled at different axial locations. The global response including fuel temperature, fuel dimensional changes, stresses, and cladding corrosion are examined.

A segment of the fuel rod at the mid-height location is also modeled using 3-D geometry to examine the detailed mechanical responses.

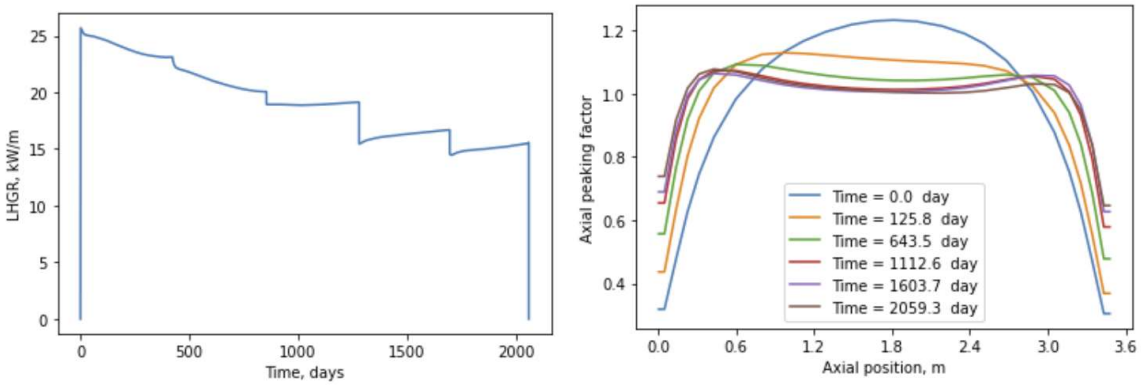

(a) Rod Avg. LHGR (b) Axial peaking factors

Figure 4: Rod power for the modeling case

3.1.1 Fuel Temperature

The temperatures at centerline, cladding valley and lobe tip locations at the mid-height position are shown in Figure 5 (a) below. The metal fuel case exhibits a much lower temperature due to the absence of a fuel-cladding gap and the high thermal conductivity of metal fuel. An equivalent cylindrical UO_2 fuel case predicts a temperature of 1600 K at beginning of life.

To examine the effects of the central displacer and the fuel design geometry on the fuel temperature prediction, a case without the displacer and an equivalent cylindrical geometry case were also run with the same linear power. Results are shown in Figure 5(b). Using a cylindrical shape without a displacer predicts a centerline temperature 66 K higher than the base case at BOL. Comparing to a helical fuel design without displacer, the centerline temperature is approximately 30 K higher than the base case.

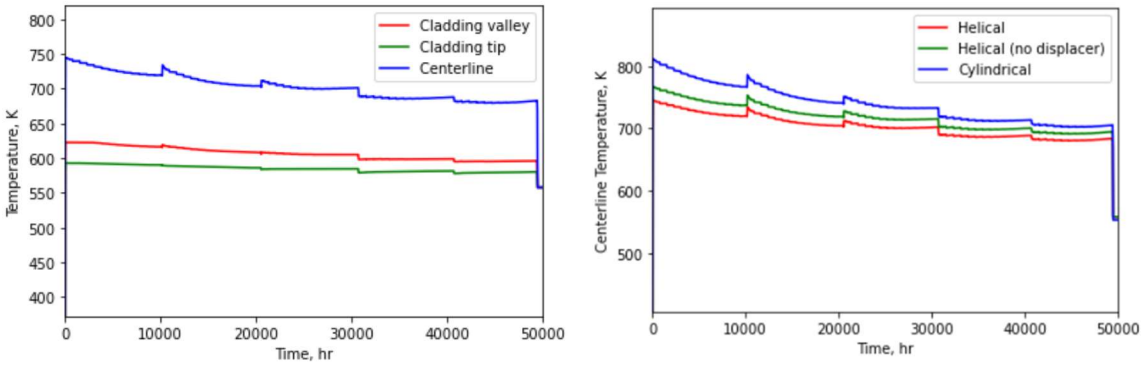

(a)Temperature at different locations (b) Temperatures with different designs

Figure 5: Temperatures predictions at different locations and with different designs

3.1.2 Cladding Corrosion

A material model for M5™ [25], which might be closer to the composition of the proposed Zr-1%Nb cladding alloy, was implemented in BISON for predicting the cladding oxidation. Figure 6 provides the maximum clad oxidation for the base case in comparison to an equivalent cylindrical UO_2 fuel design. The maximum oxide layer thickness is ~15% greater than the case with cylindrical fuel. With a 20-micron thickness of oxide, the hydrogen uptake is estimated to be ~100 ppm.

Results also shows that this fuel design, having higher heat flux at the valley location, has non-uniform oxidation predicted by the model, with the maximum oxide layer thickness predicted to be 50% greater than the minimum oxide layer thickness at the tip of the lobes.

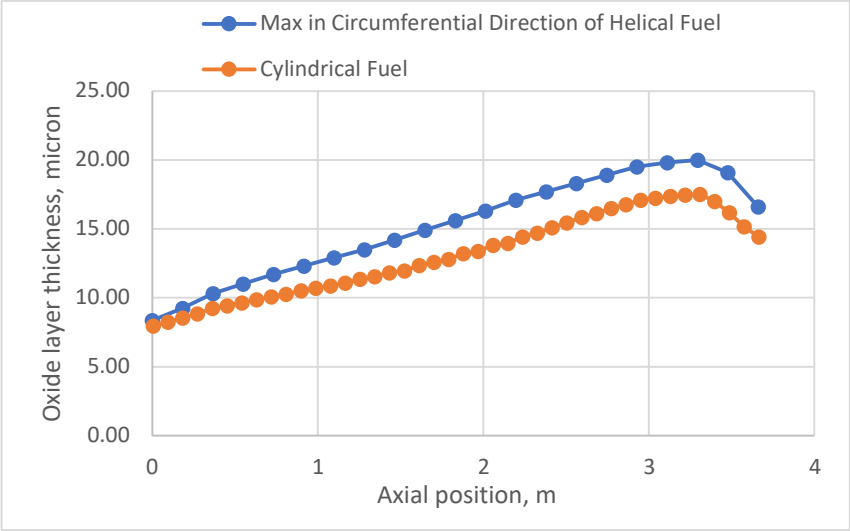

Figure 6: Axial cladding oxidation profile in comparison to cylindrical UO_2 fuel

3.1.3 Fuel Swelling

Figure 7 shows the deformed fuel geometry at the end of life (EOL) compared to the original geometry on the X-Y plane. The valley deforms more than other regions. At EOL, the radial displacement at the cladding tip is 290 microns while the radial displacement at the valley is 890 microns, roughly three times the displacement at the cladding tip.

Table 2 summarizes the fuel volume changes with different modeling options. The cladding deformation has partially accommodated the swelling of fuel core, and the total volume change is reduced by ~35% due to the constraint by cladding. The 2-D cases were run with/without contact to neighboring rods, and the rod-to-rod contact also reduces a fraction of the fuel

swelling. The dominant contribution is the solid swelling, but the gaseous swelling prediction is also appreciable, which is ~30% of the total. Assuming 1% solid swelling per 1% FIMA and neglected the gaseous swelling, the total volumetric change is reduced to 1.17 from 1.227 for the 2-D case.

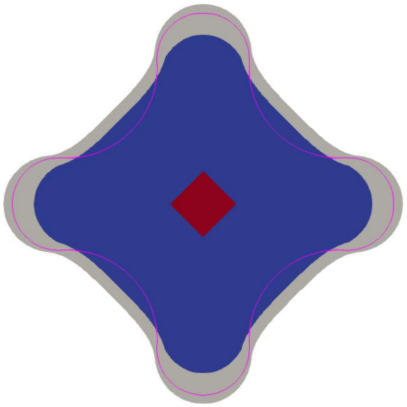

Figure 7: Fuel deformation in comparison to original contour (in pink curve)

Table 2: Fuel volume changes at EOL

	Fuel core only		Total volume	
	Solid swelling	Total swelling	Solid swelling	Total swelling
2-D[a]	1.243	1.347	1.161	1.227
2-D[a]*	1.158	1.270	1.104	1.170
2-D[b]	1.216	1.304	1.136	1.188
3-D[a]	1.252	1.372	1.170	1.250

** Using 1% volumetric strain per 1% FIMA for solid swelling; [a] No constraint; [b] Constraint from neighboring rods*
The fuel volume change is evaluated as the ratio of the fuel volume to the initial values

3.1.4 Cladding Stresses/Strains

Figure 8 show the comparison of stress evolution for constraint (rod-to-rod contact) and non-constraint cases at the valley and the tip locations respectively.

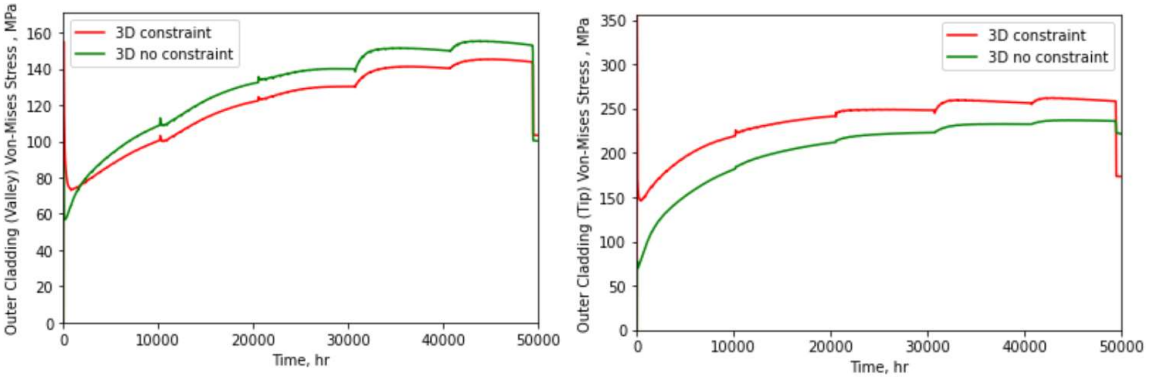

Figure 8: Cladding von-Mises stress at the valley and the tip location

The initial high stresses in the contact case are mainly caused by the fuel thermal expansion but are reduced rapidly due to the creep of fuel and cladding. Figure 9 shows the cladding hoop strain and the axial strain for the 3-D (non-constraint) case. The valley location has accumulated more creep strain than the tip location. The axial strain is lower than the deformation strains on the X-Y plane due presumably to the axial constraint by the cladding.

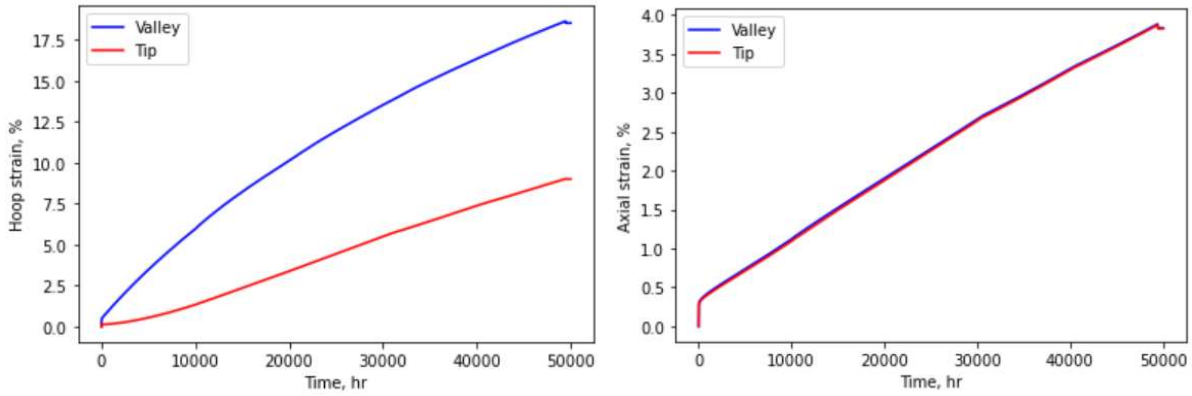

(a) (b)

Figure 9: Cladding strains at the valley and lobe tip locations: (a) hoop strain, and (b) axial strain

3.2 Results for Accident Conditions

The accident scenarios for modeling metal fuel behavior includes the loss of coolant and reactivity insertion accidents.

3.2.1 LOCA

This sub-section presents a simple analysis to compare the metallic fuel to the UO_2 fuel in a simulated LOCA condition. The reflood heat transfer correlations in BISON code are used to provide boundary conditions for the modeling case. The analysis for the metal fuel is performed using 2-D plane geometry, and the UO_2 fuel is modelled using 2-D RZ geometry.

The modeling case has the axial peaking of power at the mid-height location with a peaking factor of 1.44. Results are examined at the peak power location for both metal fuel and UO_2 fuel. Key parameters for modeling the thermal hydraulics conditions during the LOCA are summarized in Table 3 below.

Table 3: Input variables on modeling the thermal hydraulics boundary conditions

Parameter	Value
Flooding time (s)	5.0, 20.0, 60.0
Flooding rate (m/s)	0.05
Peak power, (kW/m)	30.0, 45.0
Axial location, (m)	1.88

Figure 10 shows cladding surface temperatures for UO_2 and metal fuel at various input conditions. The comparison of the peak cladding temperature in all those cases are summarized in Table 4.

Table 4: Comparison of peak cladding temperature between UO_2 fuel and UZr_2 fuel

Case	P_{max} (kW/m)*	30	45	45	45
	t_f (sec)*	5	5	20	60
PCT* (K)	UO_2	915	1000	1069	1330
	UZr_2	678	795	820	1094

**P_{max} is peak power, t_f is flooding time, and PCT is peak cladding temperature*

Under all circumstances, metal fuel has lower peak cladding temperature and shorter duration at high temperatures than UO_2 fuel. Because of the lower PCT and shorter duration at high temperatures, the cladding oxidation is also expected to be lower than UO_2 fuel. Note that the

analysis using the reflood correlation has a simple treatment of fluid temperature in the heat sink, which is assumed to be same for both UO_2 and UZr_2, and this may under-estimate the difference between the two fuels.

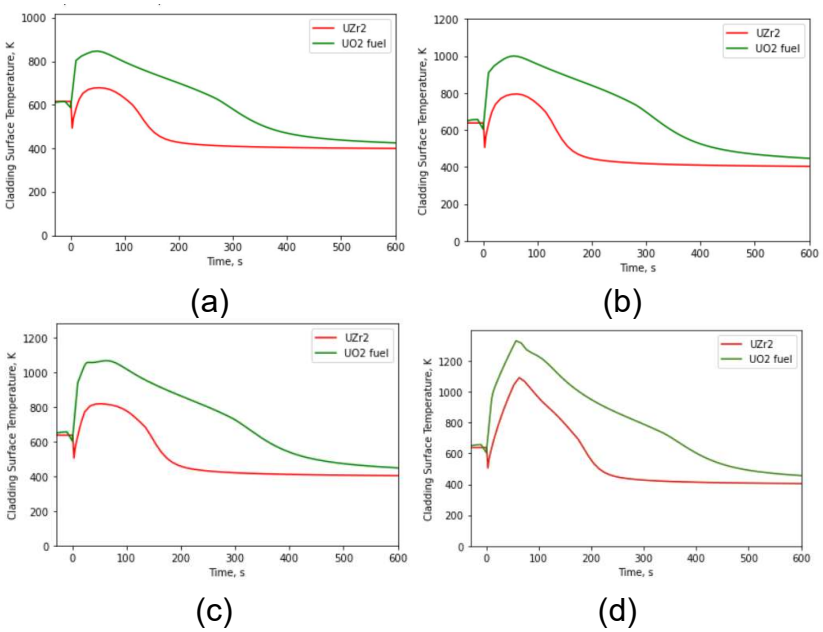

Figure 10: Cladding surface temperature during LOCA: (a) power = 30 kW/m, flooding time = 5 sec; (b) power = 45 kW/m, flooding time = 5 sec; (c) power = 45 kW/m, flooding time = 20 sec; (d) power = 45 kW/m, flooding time = 60 sec

Figure 11 shows the von-Mises stress contour of metal fuel at the peak cladding temperature time and cooling-down. The cladding stress appears to be low at the time of PCT, but increases after the fuel cooling-down due to the thermal contraction of the fuel.

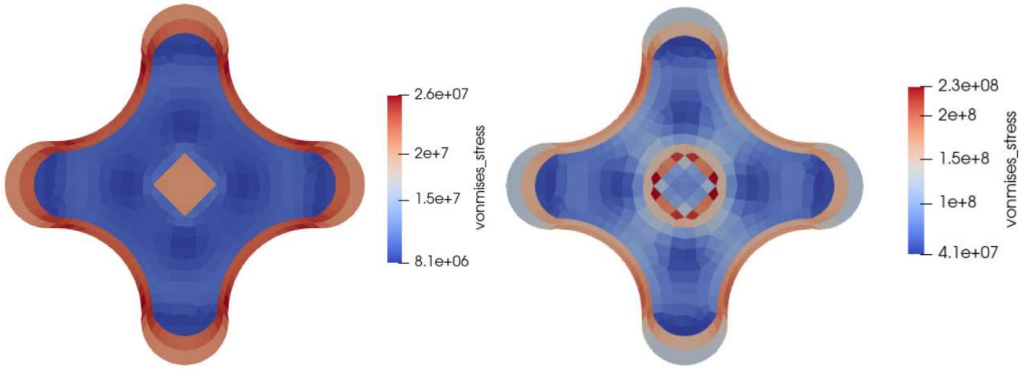

Figure 11: Von-Mises stress contour: (a) at the time of Peak Clad Temperature; (b) at the time of cooling down to 400 K (power = 45 kW/m, flooding time = 60 sec)

3.2.2 REA Modelling Results

A control rod ejection accident at hot zero power (HZP) condition is modeled with a peak power of 276,000 kW/m and pulse width of 50 ms. The maximum axial peaking factor is 2.0 (at 3.14 m) during the transient. A 3-D segment is modeled at the location of axial peaking for the examination of thermo-mechanical responses.

Figure 12 shows the peak fuel temperature, and cladding temperatures at the valley and tip locations. Figure 13 (a) shows the stress components in X, Y, and Z directions. The positive value indicates the tensile nature of the stresses. Figure 13 (b) shows the cladding hoop and axial strains at the valley locations. The peak value of hoop strain is 0.42%, slightly higher than the axial strain. For irradiated fuel, the assessment needs to account for pre-existing

stresses/strains in the cladding due to fuel swelling, and it is likely that the cladding stress may reach the yield point. However, this may still be acceptable since there would be no fission product release and fuel disposal in case of a cladding breach.

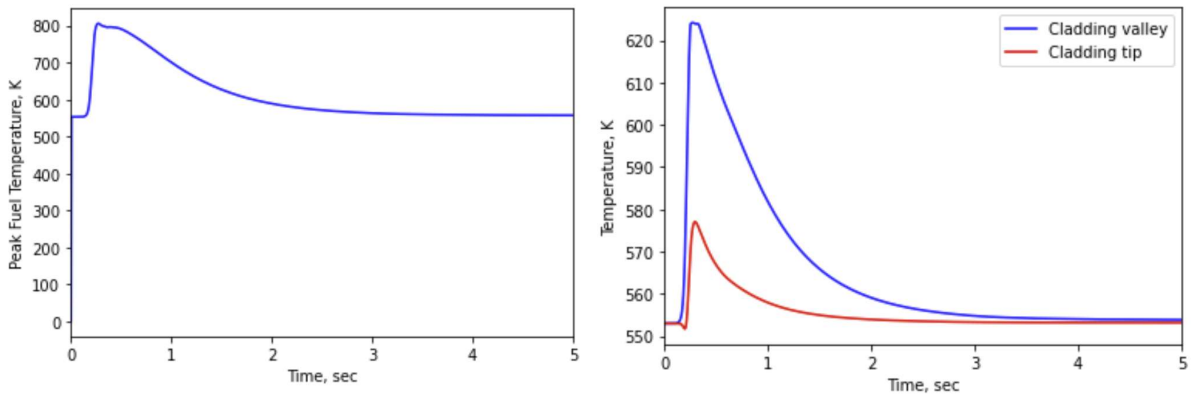

(a) (b)

Figure 12: Fuel temperature during the REA at HZP: (a) peak fuel temperature, and (b) cladding temperatures at tip and valley locations

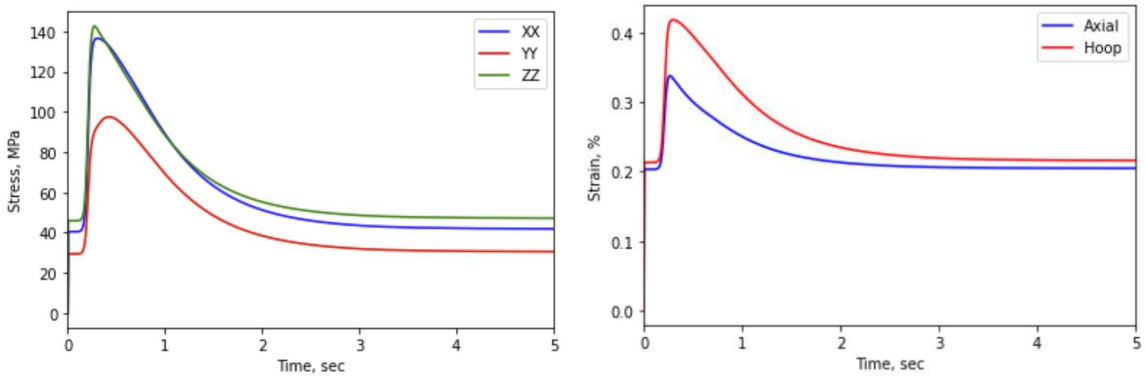

(a) (b)

Figure 13: (a) Cladding stress components at the valley location, and (b) Cladding hoop and axial strains at the valley location

4. Conclusions

The current work utilizes BISON modeling simulations to analyze the behavior of Lightbridge Corp.'s helical geometry metal fuel design in both operational and accident scenarios of LWRs. The modeling results clearly demonstrate the enhanced safety features of metallic fuel compared to ceramic UO_2 fuel, particularly under accident conditions.

The absence of free volume eliminates issues such as cladding lift-off and ballooning. The lower fuel temperatures reduce cladding oxidation during the loss-of-cooling. Although a rapid power increase in accident conditions may raise cladding stresses due to fuel thermal expansion, calculation results indicate that these stresses are not sufficient to damage the cladding.

The modeling results have also shown significant fuel dimensional changes due to swelling, which may eventually affect the economics of metal fuel utilization.

5. Acknowledgement

This research work was funded by U.S. Department of Energy (DOE) under award number DE-NE0009041. The computation conducted in the work made use of Idaho National Laboratory's High Performance Computing systems located at the Collaborative Computing Center and supported by the Office of Nuclear Energy of the U.S. DOE and the Nuclear Science User Facilities under Contract No. DE-AC07-05ID14517.

6. References

1. A. Bostrom, et. al., “Development and Properties of Uranium-Base Alloys Corrosion Resistant in High Temperature Water, Part I - Alloys without Protective Cladding,” WAPD-127, Part I, April 25, 1955
2. I. Cohen, et al., “Development and Properties of Uranium-Base Alloys Corrosion Resistant in High Temperature Water Part II – Alloys with Protective Cladding”, WAPD-127, September 1955
3. L. Bleiberg, et. al. “Development and Properties of Uranium-Base Alloys Corrosion Resistant in High Temperature Water, Part IV - Radiation Stability of Uranium-base Alloys,” WAPD-127, Part IV, May 1957
4. Willard, R.M. and Schmitt, A.R., “Irradiation Swelling, Phase Reversion, and Intergranular Cracking of U-10 wt.% Mo Fuel Alloy,” NAA-SR-8956, Atomics International, Canoga Park, CA, 1965
5. L.L.J. Marsh, Strength characteristics of zirconium-uranium alloys, in: F.A. Rough (Ed.) An Evaluation of Data on Zirconium-Uranium Alloys (Report BMI-1030), Battelle Memorial Institute, Columbus, OH, 1955, pp. 47-68
6. L.L.J. Marsh, Strength characteristics of uranium-zirconium alloys, in: A.A. Bauer (Ed.) An

   Evaluation of the Properties and Behavior of Zirconium-Uranium Alloys (Report BMI-1350), Battelle Memorial Institute, Columbus, OH, 1959, pp. 55-77
7. O. Reistad, et. al. “Russian Nuclear Power Plants for Marine Applications,” NKS-138, Apr. 2006
8. R. McDonell and E. F. Sturcken, “Development of High Performance Uranium Metal Fuels for Savanah River Reactors,” ANS Winter Meeting, San Francisco, Nov. 11-16, 1973
9. R. Montgomery, et. al., “An Innovative Accident Tolerant LWR Fuel Rod Design Based on Uranium-Molybdenum Metal Alloy,” TOPFUEL 2006
10. C. Hartmann, A. Totemeier, S. Holcomb, J. Liverad, M. Limi, J.E. Hansen and E. Navestad, *Measurement Station for Interim Inspections of Lightbridge Metallic Fuel Rods at the Halden Boiling Water Reactor,’* EPJ Web of Conferences 170, 04011 (2018)
11. Transcript of the ACRS Thermal-Hydraulics Phenomena Subcommittee, August 21, 2018, NRC-3858, ADAMS ML18254A164
12. US Patent 10,991,473 B2, Bashkirtsev et al., “Method of Manufacturing a Nuclear Fuel Assembly,” April 27, 2021
13. US Patent 2011/0255651 A1, Bashkirtsev et al., “Nuclear Reactor (Alternatives), Fuel Assembly of Seed-Blanket Subassemblies for Nuclear Reactor (Alternatives), and Fuel Element for Fuel Assembly,” Oct. 20, 2011

14. US Patent 9,355,747 B2, Bashkirtsev et al., “Light Water Reactor Fuel Assembly (Alternatives), A Light Water Reactor, and a Fuel Element of Fuel Assembly,” May 31, 2016
15. *Lightbridge Fuel™ Development Program*, ADAMS ML18232A126
16. A. Totemeier, *Lightbridge Fuel™ Overview*, Spring 2021 Nuclear Waste Technical Review Board Meeting, May 12, 2021
17. Janney, Dawn E., Metallic Fuels Handbook, Part 1: Alloys Based on U-Zr, Pu-Zr, U-Pu, or U-Pu-Zr, Including Those with Minor Actinides (Np, Am, Cm), Rare-earth Elements (La, Ce, Pr, Nd, Gd), and Y, 2018-08, INL/EXT-15-36520
18. Y.S. Touloukian, R.W. Powell, C.Y. Ho, P.G. Klemens, Thermal Conductivity (Thermophysical Properties of Matter vol. 1), IFI/Plenum, New York, 1970
19. Y. Takahashi, M. Yamawaki, K. Yamamoto, Thermophysical Properties of Uranium-Zirconium Alloys, Journal of Nuclear Materials, 154 (1988), p. 141-144
20. T.R.G. Kutty, C.B. Basak, A. Kumar, H.S. Kamath, Creep behavior of delta-phase of U-Zr system by impression creep technique, Journal of Nuclear Materials, 408 (2011), p. 90-95
21. Bagchi AC, Prasad GJ, Khan KB and Singh RP, “Physical Metallurgical Studies of Zr-Rich U-Zr Alloys,” Journal of Material Sciences and Engineering, 2013, 2:1
22. J. Malone, A. Totemeier, N. Shapiro, S. Vaidyanathan, “Lightbridge Corporation's Advanced Metallic Fuel for Light Water Reactors,” Nuclear Technology 180 (2012), p. 437–442
23. D. Pizzocri, G. Pastore, T. Barani, A. Magni, L. Luzzi, P. Van Buffelen, S.A. Pitts, A. Alfonsi, and J.D. Hales, “A Model Describing Intra-granular Fission Gas Behavior in Oxide Fuel for Advanced Engineering Tools”, Journal of Nuclear Materials, 502 (2018), p. 323-330
24. G. Pastore, N. Militello, S. Blondel, and B.D. Wirth, “Single-size and Cluster Dynamics Modeling of Intra-granular Fission Gas Bubbles in UO_2”, Journal of Nuclear Materials, 583 (2023).
25. K. Geelhood and C. Beyer, “Hydrogen Pickup Models for Zircaloy-2, Zircaloy-4, M5™ and ZIRLO™,” 2011 Water Reactor Fuel Performance Meeting, Chengdu, China, September 11-14, 2011, Paper T2-011